

Fermionic magic resources in disordered quantum spin chains

Pedro R. Nicácio Falcão^{1, 2, *}, Jakub Zakrzewski^{2, 3, †} and Piotr Sierant^{4, ‡}

¹*Szkoła Doktorska Nauk Ścisłych i Przyrodniczych,*

Uniwersytet Jagielloński, Lojasiewicza 11, PL-30-348 Kraków, Poland

²*Instytut Fizyki Teoretycznej, Wydział Fizyki, Astronomii i Informatyki Stosowanej,
Uniwersytet Jagielloński, Lojasiewicza 11, PL-30-348 Kraków, Poland*

³*Mark Kac Complex Systems Research Center, Uniwersytet Jagielloński, Kraków, Poland*

⁴*Barcelona Supercomputing Center, Barcelona 08034, Spain*

(Dated: February 3, 2026)

Fermionic non-Gaussianity quantifies a quantum state's deviation from a classically tractable free-fermionic description, constituting a necessary resource for computational quantum advantage. Here we use fermionic antiflatness (FAF) to measure this deviation across ergodic and many-body localized (MBL) regimes. We focus on the paradigmatic disordered spin-1/2 XXZ chain and its impurity variant with local interactions. Across highly excited eigenstates, FAF evolves from typical-state behavior at weak disorder to strongly suppressed values deep in the MBL regime, with volume-law scaling in the XXZ chain and an area-law bound in the impurity setting. Rare long-range catlike eigenstates exhibit a pronounced enhancement of FAF, making it a sensitive diagnostic of mechanisms proposed to destabilize MBL. Starting from product states, we find that in the MBL regime FAF grows slowly in time, approaching saturation via a power-law relaxation. Overall, our results show that MBL suppresses fermionic non-Gaussianity, and the associated complexity beyond free fermions, while ergodicity restores it, motivating explorations of fermionic non-Gaussianity in other ergodicity-breaking phenomena.

Introduction. Quantum resource theories [1] provide a framework to characterize nonclassical features of quantum states by specifying a set of free states, operations, and monotones that quantify deviations from them. When the free set is efficiently classically simulable, resource measures quantify classical description complexity and diagnose quantum computational advantage [2, 3]. A canonical example is the entanglement theory [4], where separable states are free and weakly entangled states admit efficient tensor-network representations [5–12]. Entanglement alone does not guarantee quantum advantage: even highly entangled stabilizer states [13, 14] remain efficiently simulable [15, 16], prompting the resource theory of non-stabilizerness (“magic”) [17–22].

Fermionic Gaussian states form another physically important class of efficiently simulable many-body states [23–25]. They arise from evolutions generated by Hamiltonians quadratic in Majorana operators [25, 26], or equivalently from matchgate circuits [23, 24, 27]. The covariance-matrix formalism yields efficient classical simulation of fermionic Gaussian states and provides access to equilibrium and nonequilibrium physics in a broad class of free-fermion models, including the transverse-field Ising and XY chains [28, 29]. Interactions and other non-Gaussian operations drive the state away from the Gaussian manifold [30], hindering efficient classical simulation [31–34]. This motivates the resource theory of fermionic non-Gaussianity, also termed fermionic magic resources [35–39], with fermionic Gaussian states as the free set. Measures of fermionic non-Gaussianity [35–38, 40–45] include fermionic antiflatness (FAF) [46], argued recently to be both accessible in numerics and amenable to experimental measurements.

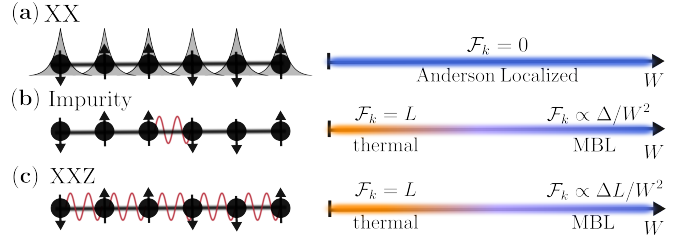


Figure 1. (a) The disordered XX chain is Anderson localized and fermionic Gaussian, hence $\mathcal{F}_k = 0$. Adding interactions $\Delta \neq 0$ gives (b) an impurity model and (c) the XXZ chain, featuring ergodic and MBL regimes with non-Gaussian eigenstates and $\mathcal{F}_k > 0$, decaying with disorder strength W as $\mathcal{F}_k \propto W^{-2}$.

Entanglement has long served as a central diagnostic of quantum many-body ground states [47–50] and nonequilibrium dynamics [51–53]. More recently, attention has increasingly turned to non-stabilizerness, with intensive studies across equilibrium phases and quantum phase transitions [54–62] and in out-of-equilibrium settings [63–77]. By comparison, studies of fermionic non-Gaussianity in many-body systems remain relatively scarce [46, 78].

Ergodic many-body systems thermalize [79, 80], dispersing local information from the initial state into entanglement and correlations throughout the system. Thermalization is accompanied by a rapid generation of fermionic non-Gaussianity [46, 81]. In this Letter we use fermionic antiflatness (FAF) to investigate how many-body localization (MBL)—a paradigmatic and robust mechanism of ergodicity breaking [82–84]—hinders the buildup of fermionic magic resources. We study the dis-

ordered spin-1/2 XXZ chain and an impurity model with local interactions (Fig. 1), which provide complementary routes from an Anderson-localized free-fermion limit to ergodic and MBL regimes. Investigating highly excited eigenstates, which underpin eigenstate-based characterizations of nonequilibrium behavior, and time evolution from product initial states, we show how disorder and interactions shape fermionic non-Gaussianity across the ergodic and MBL regimes.

Free fermions and fermionic non-Gaussianity. We study spin-1/2 chains of the form $\hat{\mathcal{H}} = \hat{\mathcal{H}}_{\text{xx}} + \hat{\mathcal{H}}_{\text{int}}$, where

$$\hat{\mathcal{H}}_{\text{xx}} = \frac{1}{4} \sum_{j=1}^L \left(\hat{\sigma}_j^x \hat{\sigma}_{j+1}^x + \hat{\sigma}_j^y \hat{\sigma}_{j+1}^y \right) + \frac{1}{2} \sum_{j=1}^L h_j \hat{\sigma}_j^z, \quad (1)$$

L is the system size, $\hat{\sigma}_j^\alpha$ (with $\alpha \in \{x, y, z\}$) are Pauli operators, $\hat{\mathcal{H}}_{\text{int}}$ is the interaction term, and the onsite fields h_j are drawn independently from a uniform distribution on $[-W, W]$, with W the disorder strength. We consider the disordered XXZ chain, a paradigmatic model for MBL studies [85–91], with Hamiltonian $\hat{\mathcal{H}}_{\text{xxz}} = \hat{\mathcal{H}}_{\text{xx}} + \hat{\mathcal{H}}_{\text{ext}}$ and interaction term $\hat{\mathcal{H}}_{\text{ext}} = \frac{\Delta}{4} \sum_{j=1}^L \hat{\sigma}_j^z \hat{\sigma}_{j+1}^z$, where Δ sets the interaction strength. In addition, we study an *impurity model* $\hat{\mathcal{H}}_{\text{imp}} = \hat{\mathcal{H}}_{\text{xx}} + \hat{\mathcal{H}}_{\text{loc}}$ with a single interacting bond, $\hat{\mathcal{H}}_{\text{loc}} = \frac{\Delta}{4} \hat{\sigma}_{L/2}^z \hat{\sigma}_{L/2+1}^z$, confined to the center of the chain.

The Jordan–Wigner mapping [92] introduces a set of $2L$ Majorana operators

$$\gamma_{2j-1} = \left(\prod_{m < j} \hat{\sigma}_m^z \right) \hat{\sigma}_j^x, \quad \gamma_{2j} = \left(\prod_{m < j} \hat{\sigma}_m^z \right) \hat{\sigma}_j^y, \quad (2)$$

which satisfy $\{\gamma_m, \gamma_n\} = 2\delta_{mn}$. In terms of these operators, the free-fermion character of $\hat{\mathcal{H}}_{\text{xx}}$ becomes explicit: it admits the quadratic Majorana form $\hat{\mathcal{H}}_{\text{xx}} = \frac{i}{4} \sum_{m,n=1}^{2L} A_{mn}^{\text{xx}} \gamma_m \gamma_n$, where A^{xx} is an $2L \times 2L$ antisymmetric, $(A^{\text{xx}})^T = -A^{\text{xx}}$, matrix [93]. Any Hermitian operator quadratic in Majoranas, $\hat{K} = \frac{i}{4} \sum_{m,n=1}^{2L} K_{mn} \gamma_m \gamma_n$ (with $K^T = -K$), generates a *fermionic Gaussian unitary* $U_K = \exp(-i\hat{K})$ [25]. Under U_K , Majorana operators transform covariantly by an orthogonal rotation, $U_K^\dagger \gamma_m U_K = \sum_{n=1}^{2L} G_{mn} \gamma_n$, with $G = \exp(K) \in \text{SO}(2L)$. Choosing G that brings A^{xx} to its canonical block-diagonal form [94, 95] yields the normal-mode decomposition $\hat{\mathcal{H}}_{\text{xx}} = \sum_{\alpha=1}^L \varepsilon_\alpha \hat{Q}_\alpha$ with $\hat{Q}_\alpha = \frac{i}{2} \tilde{\gamma}_{2\alpha-1} \tilde{\gamma}_{2\alpha}$ and $\tilde{\gamma}_m = \sum_n G_{mn} \gamma_n$. Since the operators \hat{Q}_α mutually commute, the eigenstates of $\hat{\mathcal{H}}_{\text{xx}}$ are simultaneous eigenstates of $\{\hat{Q}_\alpha\}$. Equivalently, they can be written as $U_K^\dagger |\mathbf{z}\rangle$, where $|\mathbf{z}\rangle \in \mathcal{B}$ is a $\hat{\sigma}^z$ -basis product state. Likewise, $|\psi(t)\rangle = e^{-i\hat{\mathcal{H}}_{\text{xx}}t} |\mathbf{z}\rangle$ remains fermionic Gaussian since $e^{-i\hat{\mathcal{H}}_{\text{xx}}t}$ is itself a fermionic Gaussian unitary.

Fermionic Gaussian states obey Wick's theorem [96]: all higher-order correlators factorize into sums of products of two-point functions. Accordingly, a fermionic Gaussian state $|\psi\rangle$ is fully specified by its covariance matrix $M_{mn} \equiv -\frac{i}{2} \langle \psi | [\gamma_m, \gamma_n] | \psi \rangle$, a real antisymmetric $2L \times 2L$ matrix, so storing $|\psi\rangle$ reduces to storing M .

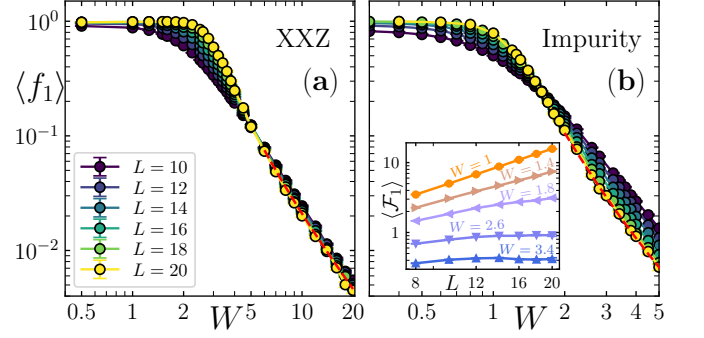


Figure 2. The FAF density $\langle f_1 \rangle$ across the ergodic–MBL crossover in (a) the XXZ chain and (b) the impurity model ($\Delta = 1$). At weak disorder W , $\langle f_1 \rangle$ approaches its typical-state value; upon entering MBL it decreases as $\langle f_1 \rangle \propto N_{\text{int}} W^{-2}$ [Eq. (4)], with a subleading W^{-4} correction (red dashed lines). Inset: $\langle \mathcal{F}_1 \rangle$ as a function of L in the impurity model for fixed W , highlighting the volume-law and area-law scalings of FAF.

Moreover, Gaussian unitaries act as orthogonal rotations of the Majorana operators, implying the covariance-matrix update $M \mapsto \hat{M} = GMG^T$. Therefore, the simulation of free-fermionic states reduces performing operations on M , with classical resources scaling only polynomially with system size L .

The interaction terms $\hat{\mathcal{H}}_{\text{ext}}$ and $\hat{\mathcal{H}}_{\text{loc}}$ are *quartic* in Majorana operators and thus break the free-fermion solvability of $\hat{\mathcal{H}}_{\text{xx}}$, driving states away from the fermionic Gaussian manifold. To quantify the fermionic non-Gaussianity of state $|\Psi\rangle$, we use the FAF [46],

$$\mathcal{F}_k(|\Psi\rangle) = L - \frac{1}{2} \text{tr}[(M^T M)^k], \quad (3)$$

where M is the covariance matrix and $k \geq 1$ is an integer. The FAF has the key properties expected of a non-Gaussianity measure [46]: it is *faithful*, $\mathcal{F}_k(|\Psi\rangle) = 0$ if and only if $|\Psi\rangle$ is fermionic Gaussian; it is *Gaussian invariant*, $\mathcal{F}_k(U_G |\Psi\rangle) = \mathcal{F}_k(|\Psi\rangle)$ for any fermionic Gaussian unitary U_G ; and it is *additive*, $\mathcal{F}_k(|\Psi\rangle \otimes |\Phi\rangle) = \mathcal{F}_k(|\Psi\rangle) + \mathcal{F}_k(|\Phi\rangle)$ if $|\Psi\rangle$ or $|\Phi\rangle$ has a fixed fermionic parity $\mathcal{P} = \prod_j \hat{\sigma}_j^z$, and subadditive otherwise. Since \mathcal{F}_k is a simple function of the two-point Majorana correlators encoded in M , FAF can be efficiently calculated numerically and is naturally suited for experiments [97–100].

Ergodic-MBL crossover. We employ the POLFED algorithm [101] to compute $n_e = \min\{100, \mathcal{N}/20\}$ mid-spectrum eigenstates of $\hat{\mathcal{H}}_{\text{xxz}}$ and $\hat{\mathcal{H}}_{\text{imp}}$ in the zero-magnetization sector of dimension $\mathcal{N} = \binom{L}{L/2}$. To obtain $\langle \mathcal{F}_k \rangle$, we average FAF over these eigenstates and over no fewer than $n_d = 1000$ disorder realizations $\{h_j\}$. The resulting FAF density $\langle f_1 \rangle = \langle \mathcal{F}_1 \rangle / L$ is shown in Fig. 2.

In the ergodic regime (weak disorder W), $\langle f_1 \rangle$ tends to unity with increasing L , consistent with the typical-state value $\mathcal{F}_k^{\text{typ}} \approx L$ [46]. In contrast, for large W , when the systems are in the MBL regime, the FAF in eigenstates is limited, similarly to entanglement [102–104] and

non-stabilizerness measures [75]. The FAF density as a function of W exhibits a crossing point that separates the ergodic and MBL regimes. For the XXZ model, the crossing point occurs around $W \approx 5$, consistent with the results obtained for the extrapolation of standard ergodicity breaking indicators [101, 105]. For the impurity model, the crossing point separating ergodic and MBL regimes occurs at $W \approx 1.6$ [106].

The behavior of $\langle f_1 \rangle$ in the MBL regimes of $\hat{\mathcal{H}}_{\text{xxz}}$ and $\hat{\mathcal{H}}_{\text{imp}}$ is markedly different. In the XXZ chain, $\mathcal{F}_1 \propto L$ yielding practically overlapping $\langle f_1 \rangle$ curves. By contrast, in the impurity model \mathcal{F}_1 becomes independent of L at large W [inset of Fig. 2(b)]. This suggests that, in the MBL regime, the scaling of \mathcal{F}_k is controlled by the spatial extent of interactions: extensive $\hat{\mathcal{H}}_{\text{ext}}$ yields extensive FAF, whereas local $\hat{\mathcal{H}}_{\text{loc}}$ yields a constant bound.

Fermionic non-Gaussianity in the MBL regime. The disordered XX chain $\hat{\mathcal{H}}_{\text{xx}}$ is a 1D free-fermion system and is Anderson localized [107, 108]. Accordingly, its normal-mode operators \hat{Q}_α are exponentially localized with localization length ξ and have dominant support on single-site operators $\hat{\sigma}_j^z$, up to corrections decaying with distance. Since $[\hat{\mathcal{H}}_{\text{xx}}, \hat{Q}_\alpha] = 0$, we view \hat{Q}_α as Anderson local integrals of motion (ALIOMs). Following [109, 110], we quantify the component of the interaction that genuinely breaks the free-fermionic structure by decomposing $\hat{\mathcal{H}}_{\text{int}}$ into parts parallel and orthogonal to the ALIOM space with respect to the Hilbert–Schmidt product $\langle \hat{A}, \hat{B} \rangle \equiv \frac{1}{N} \text{tr}[\hat{A}^\dagger \hat{B}]$ (and norm $\|\hat{A}\| = \langle \hat{A}, \hat{A} \rangle^{1/2}$): $\hat{\mathcal{H}}_{\text{int}} = \hat{\mathcal{H}}_{\text{int}}^{\parallel} + \hat{\mathcal{H}}_{\text{int}}^{\perp}$, with $\langle \hat{\mathcal{H}}_{\text{int}}^{\parallel}, \hat{\mathcal{H}}_{\text{int}}^{\perp} \rangle = 0$ and $\langle \hat{\mathcal{H}}_{\text{int}}^{\perp}, \hat{Q}_\alpha \rangle = 0$. The parallel component $\hat{\mathcal{H}}_{\text{int}}^{\parallel} = \sum_\alpha \langle \hat{\mathcal{H}}_{\text{int}}, \hat{Q}_\alpha \rangle \hat{Q}_\alpha$ produces only diagonal energy shifts, whereas $\hat{\mathcal{H}}_{\text{int}}^{\perp}$ acts as a nontrivial perturbation that breaks the fermionic Gaussianity of Anderson insulator. In the large-disorder limit, the leading contribution to $\|\hat{\mathcal{H}}_{\text{int}}^{\perp}\|$ scales as $\|\hat{\mathcal{H}}_{\text{int}}^{\perp}\| \sim \Delta N_{\text{int}}/W$, where $N_{\text{int}} = 1$ for the impurity model and $N_{\text{int}} = L$ for the XXZ chain, while $\|\hat{\mathcal{H}}_{\text{xx}}\| \sim W$; see End Matter for details.

Deep in the MBL regime, the Anderson-localized structure of $\hat{\mathcal{H}}_{\text{xx}}$ persists in the interacting system in the form of quasi-local integrals of motion (LIOMs) [103, 104, 111]. Equivalently, there exists a quasi-local unitary \hat{U} that adiabatically dresses the Anderson eigenbasis into the interacting one, so that an MBL eigenstate can be written as $|\Psi^{\text{MBL}}\rangle = \hat{U}_M |\Psi^{\text{And}}\rangle$. Writing $\hat{U}_M = e^{\hat{S}}$ with $\hat{S}^\dagger = -\hat{S}$ quasi-local, its typical magnitude is controlled by the ratio of the Gaussianity-breaking perturbation to the unperturbed bandwidth; in the large-disorder limit this yields the scaling $\|\hat{S}\| \propto \Delta N_{\text{int}}/W^2$. The dressing acts on Majorana operators by conjugation, $\tilde{\gamma}_m = \hat{U}_M^\dagger \gamma_m \hat{U}_M$, and hence on the covariance matrix of $|\Psi^{\text{MBL}}\rangle$ through $M_{mn} = -\frac{i}{2} \langle \Psi^{\text{And}} | [\tilde{\gamma}_m, \tilde{\gamma}_n] | \Psi^{\text{And}} \rangle$. For $W \gg 1$, quasi-locality implies a controlled expansion $\tilde{\gamma}_m = \gamma_m + [\gamma_m, \hat{S}] + O(\hat{S}^2)$.

This implies a decomposition $M = M_0 + \delta M$, where M_0 is the covariance matrix of $|\Psi^{\text{And}}\rangle$ and δM encodes the

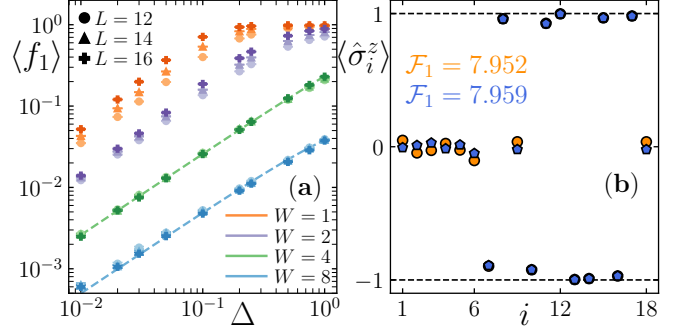


Figure 3. (a) The FAF density $\langle f_1 \rangle$ as a function of interaction strength Δ in XXZ model for different disorder strengths W and system sizes L . The dashed lines show fits $\langle f_1 \rangle = a\Delta + b\Delta^2$, with $b\Delta^2$ being a small, sub-leading correction; (b) Expectation values $\langle \hat{\sigma}_i^z \rangle$ in two long-range cat-like eigenstates of $\hat{\mathcal{H}}_{\text{xxz}}$ for $L = 18$ and $W = 14$, and the corresponding \mathcal{F}_1 values.

dressing induced by $\hat{\mathcal{H}}_\Delta^\perp$. Since Anderson eigenstate is fermionic Gaussian one has $M_0^T M_0 = \mathbb{1}$ [25], so expanding the FAF in δM yields, deep in the MBL regime,

$$\mathcal{F}_k(|\Psi^{\text{MBL}}\rangle) = \text{Tr}(M_0 \delta M) + \mathcal{O}(\|\delta M\|^2) \propto \frac{\Delta N_{\text{int}}}{W^2}, \quad (4)$$

where we retained only the leading contribution in $1/W$.

In Fig. 2 we have already observed the W^{-2} suppression of FAF deep in the MBL regime. Figure 3(a) shows $\langle f_1 \rangle$ versus interaction strength Δ for several disorder values W . At large W , $\langle f_1 \rangle$ follows the perturbative scaling $\mathcal{F}_1 \propto \Delta$ with high accuracy, consistent with a smooth dressing of Anderson-localized free-fermion eigenstates at $\Delta = 0$ into interacting eigenstates in the MBL regime, with non-Gaussianity controlled by Δ . In contrast, at weak disorder (e.g., $W = 1$) even small interactions lead to a pronounced growth of $\langle f_1 \rangle$ with system size L , signaling an instability of the Anderson insulator and the onset of ergodicity. In the thermodynamic limit this behavior is consistent with a nonanalytic dependence on Δ , with FAF jumping from $\mathcal{F}_1 = 0$ at $\Delta = 0$ to an extensively scaling value set by the typical-state behavior $\langle f_1 \rangle \simeq 1$.

Cat-like eigenstates. While mathematical constructions [112, 113] support the existence of a quasilocal dressing unitary \hat{U}_M at sufficiently large disorder W (even in the thermodynamic limit), the fate of the ergodic–MBL crossover as $L \rightarrow \infty$ remains debated [84]. A widely discussed mechanism for destabilizing MBL involves rare many-body resonances [114–121], which evade a simple adiabatic connection to Anderson eigenstates. In this scenario, interactions hybridize two spin configurations that differ over a macroscopic region, producing a cat-like superposition on that segment while the remaining degrees of freedom stay effectively frozen [119]. Such resonant eigenstates can occur even deep in the MBL regime and are visible in spin correlations [119, 122]: their longitudinal connected correlator

$C_{i,i+L/2}^{zz} = |\langle \hat{\sigma}_i^z \hat{\sigma}_{i+L/2}^z \rangle - \langle \hat{\sigma}_i^z \rangle \langle \hat{\sigma}_{i+L/2}^z \rangle|$ remains $O(1)$ even at $W \gg 1$, whereas $C_{i,i+L/2}^{zz} \approx 0$ for typical eigenstates.

In Fig. 3(b) we show the profiles $\langle \hat{\sigma}_i^z \rangle$ for a pair of representative long-range resonant eigenstates deep in the MBL regime. The $\langle \hat{\sigma}_i^z \rangle$ profiles suggest an ansatz [119]

$$|\Psi_{\text{cat}}^\pm\rangle = |\varphi\rangle \otimes |\Psi_{\text{fr}}\rangle, \quad (5)$$

where $|\Psi_{\text{fr}}\rangle$ is a product state on the nonresonant sites with $\langle \hat{\sigma}_i^z \rangle = \pm 1$, and $|\varphi\rangle = \frac{1}{\sqrt{2}}(|\uparrow, \downarrow, \uparrow, \downarrow, \dots\rangle \pm |\downarrow, \uparrow, \downarrow, \uparrow, \dots\rangle)$ is a cat superposition on the resonant segment. Due to FAF additivity, $\mathcal{F}_k(|\Psi_{\text{cat}}^\pm\rangle) = \mathcal{F}_k(|\varphi\rangle) + \mathcal{F}_k(|\Psi_{\text{fr}}\rangle)$. Since $|\Psi_{\text{fr}}\rangle$ is fermionic Gaussian (hence $\mathcal{F}_k(|\Psi_{\text{fr}}\rangle) = 0$), FAF isolates the contribution of the cat component. The cat state $|\varphi\rangle$ has vanishing covariance matrix, and $\mathcal{F}_k(|\varphi\rangle)$ is equal to the number of spins participating in the many-body resonance. Consistently, for the states in Fig. 3(b) we find $\mathcal{F}_1 \approx 7.95$, in close agreement with the size of the resonant region inferred from $\langle \hat{\sigma}_i^z \rangle$.

These results show that many-body resonances, a leading candidate mechanism for destabilizing MBL, are accompanied by a pronounced enhancement of fermionic non-Gaussianity: cat-like resonant eigenstates exhibit much larger FAF than typical eigenstates at the same disorder, demonstrating the direct link between nonperturbative mechanisms destabilizing MBL and fermionic magic resources. At present, the impact of such rare resonances on the fate of MBL in the thermodynamic limit remains unresolved, since at numerically accessible system sizes long-range resonant states occur with low probability. In contrast, at the ergodic–MBL crossover (e.g., $W = 5$ in the XXZ chain) the dominant resonances are typically short-ranged, involving ~ 4 sites and producing a peak around $\mathcal{F}_k \approx 4$ in the FAF distribution; a quantitative analysis of resonance statistics, including longer-range events, is presented in [123].

Time dynamics. Finally, we investigate the real-time dynamics of the FAF in the MBL regime. We compute the time-evolution operator $U(t) = e^{-i\hat{\mathcal{H}}t}$ by full exact diagonalization of $\hat{\mathcal{H}}_{\text{XXZ}}$ and $\hat{\mathcal{H}}_{\text{imp}}$ with open boundary conditions. We calculate the FAF of time-evolved state $|\Psi_t\rangle = U(t)|\Psi_0\rangle$ with an initial Néel state $|\Psi_0\rangle = |\uparrow, \downarrow, \dots, \uparrow, \downarrow\rangle$, and average the results over 10^4 disorder realizations to obtain the average FAF, $\langle \mathcal{F}_1(|\Psi_t\rangle) \rangle$.

The results for $\langle \mathcal{F}_1 \rangle$ in the MBL regime of the XXZ chain are shown in Fig. 4(a) for system size $L = 10, \dots, 16$. The initial Néel product state is fermionic Gaussian, hence $\langle \mathcal{F}_1(|\Psi_0\rangle) \rangle = 0$. In contrast to ergodic dynamics, where FAF grows rapidly and saturates on timescales set by L [46], in the MBL regime $\langle \mathcal{F}_1 \rangle$ increases slowly over several decades in time, reminiscent of the slow entanglement growth phenomenology at strong disorder [124–128]. An analogous slow growth is observed in the impurity model at $W = 3$ [Fig. 4(b)]. At fixed intermediate times (e.g., $t = 10$), the system-size dependence differs: in the XXZ chain $\langle \mathcal{F}_1 \rangle$ grows approximately linearly with L ,

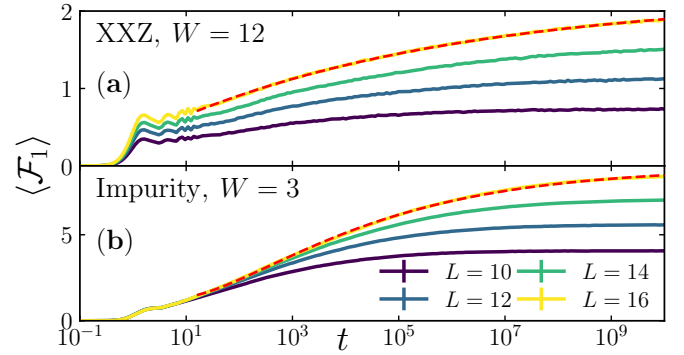


Figure 4. Time dynamics of $\langle \mathcal{F}_1 \rangle$ for the (a) XXZ and (b) impurity model in the MBL regime, with interaction strength set as $\Delta = 1$. The evolution of $\langle \mathcal{F}_1 \rangle$ follows the prediction in Eq. (7), as shown by the red-dashed lines; in the impurity model the second-order term $t^{-2\beta}$ is non-negligible.

while in the impurity model it is nearly L independent. Nevertheless, the long-time saturation value is extensive in L in *both* models, paralleling the volume-law saturation of entanglement entropy [124–128].

To understand the FAF dynamics in the MBL regime, we note that Eq. (3) implies

$$\mathcal{F}_1(|\Psi_t\rangle) = L - \sum_{m < n} |\langle \gamma_m \gamma_n \rangle|_t^2, \quad (6)$$

so $\langle \mathcal{F}_1 \rangle$ is governed by two-point Majorana correlators in the time-evolved state $|\Psi_t\rangle$. Deep in MBL these correlators exhibit slow relaxation. The onsite bilinears $\gamma_m \gamma_n$ with $(m, n) = (2k-1, 2k)$ reduce (up to a constant factor) to $|\langle \hat{\sigma}_k^z \rangle|_t^2$, which approaches a constant $c_z < 1$ with a power-law decay [84]. The nonlocal bilinears with $|m - n| > 1$ map under Eq. (2) to $\hat{\sigma}_i^\alpha (\prod_{j=i+1}^{l-1} \hat{\sigma}_j^z) \hat{\sigma}_l^\alpha$ (with $\alpha \in \{x, y\}$, $i = \lfloor \frac{m}{2} \rfloor$, and $l = \lfloor \frac{n}{2} \rfloor$), whose expectation values decay as $|\langle \gamma_m \gamma_n \rangle|_t^2 \sim t^{-A\beta}$, where β is a constant and $A = 2$ at short times and crossing over to $A = 1$ once the endpoint spins become entangled (see End Matter). Hence, the double sum in Eq. (6) can be organized by distance $|m - n|$: the onsite terms yield the contribution Lc_z , while the remaining terms provide power-law corrections. As a result,

$$\mathcal{F}_1(|\Psi_t\rangle) = \mathcal{F}_1^{\text{MBL}} - C t^{-\beta} + O(t^{-2\beta}), \quad (7)$$

where $\mathcal{F}_1^{\text{MBL}} = L(1 - c_z)$ is the extensive long-time saturation value, set by the initial state and disorder strength, β is fixed by the decay of Majorana correlators, and C is a constant. The fits in Fig. 4 for both the XXZ and impurity models are consistent with Eq. (7).

Conclusion. In this work we characterized fermionic magic resources in out-of-equilibrium disordered spin-1/2 chains. By analyzing highly excited eigenstates, we found that at strong disorder the MBL regime remains smoothly connected to the free-fermionic Anderson-insulator limit: fermionic non-Gaussianity is suppressed

as disorder increases, and its scaling is set by the amplitude and spatial extent of the interactions. The rare long-range cat-like resonance eigenstates, while having negligible weight in disorder-averaged observables at accessible sizes, exhibit a pronounced enhancement of fermionic non-Gaussianity, tying candidate nonperturbative mechanisms for destabilizing MBL to beyond free-fermion state complexity. At weak disorder, in contrast, interactions destabilize the Anderson limit and drive the system into an ergodic regime where fermionic non-Gaussianity approaches typical-state values with increasing system size. These eigenstate trends are mirrored in dynamics: deep in MBL, fermionic non-Gaussianity grows anomalously slowly and relaxes toward an extensive plateau via a power-law in time.

We conjecture that the phenomenology of fermionic magic resources established here extends to a broader class of systems that exhibit MBL and admit a well-defined localized free-fermion limit, including models with quasiperiodic potentials [129–133], disorder-free localization [134–140], and disordered Ising chains [141]. In the End Matter we further support this conjecture by showing that a LIOM description [103, 104] reproduces the FAF behavior observed in our results. More broadly, our results provide a reference point for future studies of fermionic non-Gaussianity in other mechanisms

of nonergodicity, including disorder-induced regimes beyond simple LIOM phenomenology such as bond disorder [142] and random interactions [143], and other nonergodic phenomena such as many-body scars [144–148] and ergodicity breaking due to gauge constraints [149] or other conservation laws [150]. We leave for future work the question of how ergodicity breaking in these settings constrains fermionic magic resources and quantum-state complexity.

Acknowledgments. We acknowledge insightful discussions with Konrad Pawlik. P.S. acknowledges collaboration with Sreemayee Aditya, Paolo Stornati, Emanuele Tirrito, and Xhek Turkeshi on related topics, and useful discussions with members of Quantic group at BSC. The work of P.R.N.F. and J.Z. was funded by the National Science Centre, Poland, project 2021/43/I/ST3/01142 – OPUS call within the WEAVE programme. P.S. acknowledges fellowship within the “Generación D” initiative, Red.es, Ministerio para la Transformación Digital y de la Función Pública, for talent attraction (C005/24-ED CV1), funded by the European Union NextGenerationEU funds through PRTR. We gratefully acknowledge the Polish high-performance computing infrastructure PLGrid (HPC Centers: ACK Cyfronet AGH) for providing computer facilities and support within the computational grant no. PLG/2025/018400.

End Matter

Phenomenological description of MBL. Deep in the MBL regime, interacting disordered models can be described with good accuracy by an extensive set of quasi-local integrals of motion (LIOMs), also known as ℓ -bits (localized bits) [103, 104, 111]. Within this phenomenological framework, the effective Hamiltonian takes the form

$$\hat{\mathcal{H}}_{\ell\text{-bit}} = \sum_i h_i \hat{\tau}_i^z + \sum_{i < j} J_{ij} \hat{\tau}_i^z \hat{\tau}_j^z + \sum_{i < j < k} J_{ijk} \hat{\tau}_i^z \hat{\tau}_j^z \hat{\tau}_k^z + \dots \quad (8)$$

where h_i are on-site random fields, reminiscent of the normal-mode decomposition of the XX model [Eq. (1)], and the interactions decay exponentially with the distance between the ℓ -bits, $J_{ij} \sim J_0 e^{-|i-j|/\xi'}$, with ξ' setting the interaction range and J_0 the interaction scale. The Hamiltonian (8) captures several properties of the MBL regime [151–156], and constructive schemes to find the ℓ -bits have been developed, e.g., in the XXZ chain [157, 158].

Here, we employ a $U(1)$ -symmetric circuit \hat{U}_ℓ that maps the ℓ -bit basis to the $\hat{\sigma}^z$ -basis [153]. The circuit is arranged in a brickwork structure, with a depth of D_u , where each two-site gate \hat{U}_i is a random 4×4 Hermitian operator of the form $\hat{U}_i = e^{-ifw_i\hat{F}_i}$, with $w_i = e^{-2|h_i-h_{i+1}|}$

suppressing the spread of correlations, and

$$\hat{\Gamma}_i = \frac{\theta_1}{2} \hat{\sigma}_i^z + \frac{\theta_2}{2} \hat{\sigma}_{i+1}^z + \frac{\theta_3}{2} \lambda \hat{\sigma}_i^z \hat{\sigma}_{i+1}^z + c \hat{\sigma}_i^+ \hat{\sigma}_{i+1}^- + c^* \hat{\sigma}_i^- \hat{\sigma}_{i+1}^+ \quad (9)$$

where $\hat{\sigma}_j^\pm = \frac{1}{2}(\hat{\sigma}_j^x \pm i\hat{\sigma}_j^y)$, and $\{\theta_1, \theta_2, \theta_3, \mathbb{R}(c), \mathbb{I}\mathfrak{m}(c)\} \in \mathcal{N}(0, 1)$ are independent random variables drawn from a normal distribution with zero mean and unit variance. The parameter f controls the localization length and serves as an effective disorder strength.

The ℓ -bit operators are related to the physical spin operators by the quasi-local unitary \hat{U}_ℓ , i.e., $\hat{\tau}_k^\alpha = \hat{U}_\ell \hat{\sigma}_k^\alpha \hat{U}_\ell^\dagger$, with $\alpha \in \{x, y, z\}$. As a consequence, a local spin operator along the $\hat{\sigma}^z$ -direction can be written as

$$\hat{\sigma}_k^z = \sum_{k_1} B_{k_1} \hat{\tau}_{k_1}^z + \sum_{k_1, k_2, \alpha'} B_{k_1 k_2}^{\alpha' \alpha'} \hat{\tau}_{k_1}^{\alpha'} \hat{\tau}_{k_2}^{\alpha'} + \dots \quad (10)$$

with $\alpha' \in \{x, y, z\}$. The quasi-locality of the ℓ -bit operators guarantees that the coefficients B_k decay exponentially with the distance between the physical site k and the ℓ -bit indices. Additionally, the operators $\hat{\tau}^\alpha$ are chosen such that $[\hat{\sigma}_k^z, \sum_{k'} \hat{\tau}_{k'}^z] = 0$.

We now investigate the dynamics of the Majorana operators and provide a complete derivation of Eq. (7). For $k = 1$, the FAF is given by Eq. (6). The two-point Majorana correlators can be expressed as a Pauli

string, $\gamma_m \gamma_n = \hat{\sigma}_i^\alpha \left(\prod_{j=i+1}^{l-1} \hat{\sigma}_j^z \right) \hat{\sigma}_l^{\alpha'}$, with $(\alpha, \alpha') \in \{x, y\}$, $i = \lfloor m/2 \rfloor$, and $l = \lfloor n/2 \rfloor$. For Majoranas acting on the same physical site, this expression reduces to a local $\hat{\sigma}^z$ operator. In contrast, for distinct sites, it corresponds to a nonlocal string with two nontrivial $(\hat{\sigma}^x, \hat{\sigma}^y)$ operators connected by a parity string.

It is crucial to first understand the dynamics of the ℓ -bit operators under the dynamics of Eq. (8) and, subsequently, map these results back to spin operators using Eq. (10). Within the ℓ -bit framework, we have that $\langle \hat{\tau}_k^z(t) \rangle = \langle \hat{\tau}_k^z(0) \rangle$. In contrast, off-diagonal operators exhibit algebraic decay, with distinct exponents depending on whether the corresponding ℓ -bits are entangled [151]

$$|\langle T_{ij}^{\alpha\alpha'}(t) \rangle| \propto \begin{cases} 1/t^{2\beta}, & t \ll J_0^{-1} e^{|i-j|/\xi} \\ 1/t^\beta, & t \gg J_0^{-1} e^{|i-j|/\xi} \end{cases} \quad (11)$$

where $T_{ij}^{\alpha\alpha'} = \hat{\tau}_i^\alpha \hat{\tau}_j^{\alpha'}$. Here, ξ is the effective localization length of the ℓ -bits and $\beta \leq \xi \ln 2$. These two different dynamical regimes allow us to write

$$\mathcal{F}_1(|\Psi_t\rangle) = (L - c_z) - \sum_{m=1}^{2L} \sum_{n=m+2}^{2L} |\langle \gamma_m \gamma_n \rangle_t|^2 \quad (12)$$

where $c_z = \sum_{k=1}^L |\langle \hat{\sigma}_k^z \rangle_t|^2$. The first term on the r.h.s. has a significant overlap with $\hat{\tau}^z$'s operators and, therefore, controls the saturation value $\mathcal{F}_1^{\text{MBL}}$. Nevertheless, the second term on the r.h.s of Eq. (10) guarantees a small power-law decay before reaching its saturation value. The latter term of Eq. (12) exhibits similar power-law behavior, although with a much smaller saturation value.

The power-law exponent of Eq. (11) depends on whether a given pair of ℓ -bits is entangled. For a pair separated by a distance $r = |i - j|$, entanglement only builds up after a time $t^* \approx e^{r^*/\xi}$. Consequently, the FAF assumes the form

$$\mathcal{F}_1(|\Psi(t)\rangle) = \mathcal{F}_1^{\text{MBL}} - \sum_{r=1}^{\lfloor r^* \rfloor} A_1(r) t^{-\beta} - \sum_{r=\lceil r^* \rceil} A_2(r) t^{-2\beta} \quad (13)$$

where the coefficients $A_{1,2}(r)$ encode the exponentially suppressed contributions of distant ℓ -bit pairs and depend only on the distance between the spins.

We now investigate the time dynamics of two-point Majorana correlators in the MBL regime, comparing the phenomenological ℓ -bit description with the microscopic XXZ model. In both systems, we consider an initial Néel state and evolve the system using exact methods. As shown in Fig. 5(a,b), the dynamics of Majoranas are aligned in both models: In the noninteracting limit ($\Delta = 0$ for XXZ and $\lambda = 0$ for ℓ -bit), the correlators $|\langle \gamma_m \gamma_n \rangle|^2$ rapidly saturate to a constant, with the value depending on whether we consider a local $\hat{\sigma}^z$ operator [panel (a)] or a non-local string [panel (b)]. In contrast,

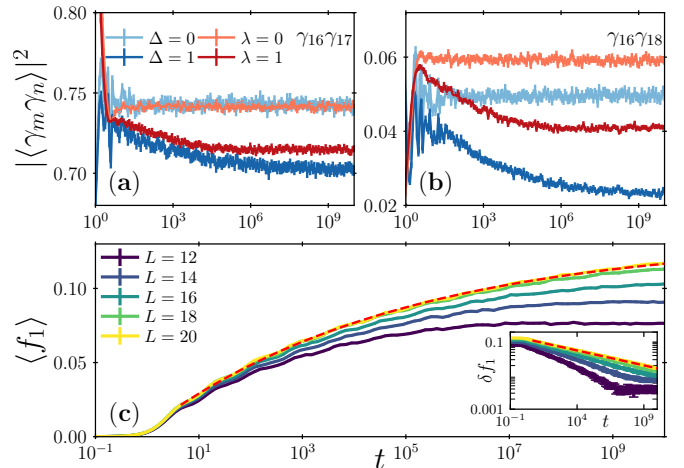


Figure 5. (a-b) Time-evolution of Majorana correlators $|\langle \gamma_m \gamma_n \rangle|^2$ in the MBL regime for the XXZ Hamiltonian (blue) and the ℓ -bit model (red) for $L = 16$ and $W = 12$ (for the XXZ model). In the noninteracting case ($\Delta = \lambda = 0$, light colors), the correlators rapidly saturate to a constant, reflecting trivial dynamics. In contrast, in the interacting case ($\Delta = \lambda = 1$, dark colors), spin dephasing induces a slow power-law decay prior to saturation. (c) Dynamics of $\langle f_1 \rangle$ for the ℓ -bit Hamiltonian at $\lambda = 1$ for several system sizes L . The dynamics display a clear power-law behavior (red-dashed line), consistent with Eq. (13). Inset: Time-evolution of $\delta f_1 = f_1^{\text{MBL}} - \langle f_1 \rangle$, highlighting the same power-law behavior.

interactions ($\Delta = \lambda = 1$, dark colors) induce a slow power-law decay over several decades in time before saturation, a hallmark of MBL dynamics. Since the FAF dynamics are directly inherited from the underlying Majorana correlators, the same power-law behavior is expected to govern their time dependence.

Figure 5(c) shows the time evolution of the FAF density $\langle f_1 \rangle$ for several system sizes L at fixed $\xi' = 0.5$ and $\lambda = 1$. The FAF exhibits a clear, extensive growth with the system size L , and its dynamical behavior is well captured by the phenomenological description of Eq. (13). A fit of the $L = 20$ data using Eq. (7) yields excellent agreement (red dashed-line), with fitted parameters $f_1^{\text{MBL}} \approx 0.133$ and $\beta \approx 0.09$. The inset further highlights the power-law relaxation, showing that $\delta f_1 = f_1^{\text{MBL}} - \langle f_1 \rangle$ decays algebraically in time.

Interacting Hamiltonians in the Anderson basis. Upon Jordan-Wigner transformation (2), the XX Hamiltonian (1) admits a free-fermion representation,

$$\hat{\mathcal{H}}_{\text{xx}} = \frac{i}{4} \sum_{j=1}^L \eta_j (\gamma_{2j-1} \gamma_{2j+2} - \gamma_{2j} \gamma_{2j+1}) - \frac{i}{2} \sum_{j=1}^L h_j \gamma_{2j-1} \gamma_{2j} \quad (14)$$

with $\eta_j = 1$ for $j \neq L$ and $\eta_L = \pm 1$ is fixed by the fermionic parity sector. As discussed in the main text, one can define a transformation such that the XX Hamiltonian can be written in its normal-mode decomposition, i.e., $\hat{\mathcal{H}}_{\text{xx}} = \sum_{\alpha=1}^L \varepsilon_\alpha \hat{Q}_\alpha$, with $\hat{Q}_\alpha = \frac{i}{2} \tilde{\gamma}_{2\alpha-1} \tilde{\gamma}_{2\alpha}$ (see main text

for definitions). The operators \hat{Q}_α are conserved quantities that define the Anderson local integrals of motion (ALIOMs).

To express the interacting disordered Hamiltonians in the ALIOM basis, we introduce new fermionic operators $\hat{f}_\alpha = \frac{1}{2}(\tilde{\gamma}_{2\alpha-1} + i\tilde{\gamma}_{2\alpha})$, satisfying $\{\hat{f}_\alpha, \hat{f}_\beta^\dagger\} = \delta_{\alpha\beta}$ and $\hat{Q}_\alpha = \hat{f}_\alpha^\dagger \hat{f}_\alpha - \frac{1}{2}$. In terms of these modes, the interacting contribution of the XXZ Hamiltonian takes the form $\hat{\mathcal{H}}_{\text{ext}} = \sum_{k,l,m,n} U_{\text{ext}}^{k,l,m,n} \hat{f}_k^\dagger \hat{f}_l \hat{f}_m^\dagger \hat{f}_n$ and, as shown in Ref. [159], $\hat{\mathcal{H}}_{\text{ext}}$ can be decomposed into four different contributions,

$$\begin{aligned} \hat{\mathcal{H}}_{\text{ext}} = & \sum_{k=1}^L \mathcal{U}_k^{(1)} \hat{Q}_k + \sum_{k \neq l} \mathcal{U}_{k,l}^{(2)} \hat{Q}_k \hat{Q}_l \\ & + \sum_{k \neq l \neq m} \mathcal{U}_{k,l,m}^{(3)} \hat{Q}_k \hat{f}_l^\dagger \hat{f}_m + \sum_{k \neq l \neq m \neq n} \mathcal{U}_{k,l,m,n}^{(4)} \hat{f}_k^\dagger \hat{f}_l \hat{f}_m^\dagger \hat{f}_n \end{aligned} \quad (15)$$

where the first line of Eq. (15) commutes with the ALIOMs, while the second line constitutes the genuine perturbation of the XX model.

The off-diagonal terms of Eq. (15) decay exponentially with the distance between the involved orbitals and are therefore dominated by maximally overlapping configurations. The leading contributions act on successive sites and scale as

$$\mathcal{U}_{k,k+1,k+2}^{(3)} \propto \Delta/W \quad (16)$$

$$\mathcal{U}_{k,k+1,k+2,k+3}^{(4)} \propto \Delta/W^2 \quad (17)$$

Since these terms do not commute with the ALIOMs, they constitute, in the perturbative picture, the source of the generation of fermionic magic resources in disordered systems. The leading contribution to the norm of the true perturbation decays as presented in [110], yielding the FAF scaling presented in Eq. (4).

A similar representation can be obtained for the interacting term in the impurity model, $\hat{\mathcal{H}}_{\text{loc}}$. However, the presence of confined interactions in the Hamiltonian limits the expansion of the interacting terms only to the sites nearby $L/2$, resulting in an *area-law* scaling of the FAF.

-
- * pedro.nicaciofalcao@doctoral.uj.edu.pl
 † jakub.zakrzewski@uj.edu.pl
 ‡ piotr.sierant@bsc.es
- [1] E. Chitambar and G. Gour, Quantum resource theories, *Rev. Mod. Phys.* **91**, 025001 (2019).
 [2] J. Preskill, Quantum computing and the entanglement frontier (2012), [arXiv:1203.5813 \[quant-ph\]](https://arxiv.org/abs/1203.5813).
 [3] A. J. Daley, I. Bloch, C. Kokail, S. Flannigan, N. Pearson, M. Troyer, and P. Zoller, Practical quantum advantage in quantum simulation, *Nature* **607**, 667 (2022).
 [4] R. Horodecki, P. Horodecki, M. Horodecki, and K. Horodecki, Quantum entanglement, *Rev. Mod. Phys.* **81**, 865 (2009).
 [5] G. Vidal, Efficient classical simulation of slightly entangled quantum computations, *Phys. Rev. Lett.* **91**, 147902 (2003).
 [6] F. Verstraete, J. J. García-Ripoll, and J. I. Cirac, Matrix product density operators: Simulation of finite-temperature and dissipative systems, *Phys. Rev. Lett.* **93**, 207204 (2004).
 [7] F. Verstraete, V. Murg, and J. Cirac, Matrix product states, projected entangled pair states, and variational renormalization group methods for quantum spin systems, *Adv. Phys.* **57**, 143 (2008).
 [8] R. Orús, A practical introduction to tensor networks: Matrix product states and projected entangled pair states, *Ann. Phys.* **349**, 117 (2014).
 [9] J. Haegeman, C. Lubich, I. Oseledets, B. Vandereycken, and F. Verstraete, Unifying time evolution and optimization with matrix product states, *Phys. Rev. B* **94**, 165116 (2016).
 [10] R. Orús, Tensor networks for complex quantum systems, *Nat. Rev. Phys.* **1**, 538 (2019).
 [11] S.-J. Ran, E. Tirrito, C. Peng, X. Chen, L. Tagliacozzo, G. Su, and M. Lewenstein, *Tensor network contractions: methods and applications to quantum many-body systems* (2020).
 [12] M. C. Bañuls, Tensor network algorithms: A route map, *Annu. Rev. Condens. Matter Phys.* **14**, 173–191 (2023).
 [13] G. Smith and D. Leung, Typical entanglement of stabilizer states, *Phys. Rev. A* **74**, 062314 (2006).
 [14] O. Dahlsten and M. B. Plenio, Exact entanglement probability distribution of bi-partite randomised stabilizer states (2007), [arXiv:quant-ph/0511119 \[quant-ph\]](https://arxiv.org/abs/quant-ph/0511119).
 [15] D. Gottesman, The heisenberg representation of quantum computers (1998), [arXiv:quant-ph/9807006 \[quant-ph\]](https://arxiv.org/abs/quant-ph/9807006).
 [16] S. Aaronson and D. Gottesman, Improved simulation of stabilizer circuits, *Phys. Rev. A* **70**, 052328 (2004).
 [17] V. Veitch, C. Ferrie, D. Gross, and J. Emerson, Negative quasi-probability as a resource for quantum computation, *New Journal of Physics* **14**, 113011 (2012).
 [18] V. Veitch, S. A. H. Mousavian, D. Gottesman, and J. Emerson, The resource theory of stabilizer quantum computation, *New J. Phys.* **16**, 013009 (2014).
 [19] M. Howard and E. Campbell, Application of a resource theory for magic states to fault-tolerant quantum computing, *Phys. Rev. Lett.* **118**, 090501 (2017).
 [20] X. Wang, M. M. Wilde, and Y. Su, Quantifying the magic of quantum channels, *New J. Phys.* **21**, 103002 (2019).
 [21] Z.-W. Liu and A. Winter, Many-body quantum magic, *PRX Quantum* **3**, 020333 (2022).
 [22] L. Leone, S. F. E. Oliviero, and A. Hamma, Stabilizer Rényi entropy, *Phys. Rev. Lett.* **128**, 050402 (2022).
 [23] L. G. Valiant, Quantum computers that can be simulated classically in polynomial time, in *Proceedings of the Thirty-Third Annual ACM Symposium on Theory of Computing*, STOC '01 (Association for Computing Machinery, New York, NY, USA, 2001) p. 114–123.
 [24] B. M. Terhal and D. P. DiVincenzo, Classical simulation of noninteracting-fermion quantum circuits, *Phys. Rev. A* **65**, 032325 (2002).
 [25] S. Bravyi, Lagrangian representation for fermionic linear optics, *Quantum Info. Comput.* **5**, 216–238 (2005).
 [26] E. Majorana and L. Maiani, A symmetric theory of electrons and positrons, in *Ettore Majorana Scientific Pa-*

- pers: *On occasion of the centenary of his birth*, edited by G. F. Bassani (Springer Berlin Heidelberg, Berlin, Heidelberg, 2006) pp. 201–233.
- [27] R. Jozsa and A. Miyake, Matchgates and classical simulation of quantum circuits, *Proc. R. Soc. A Math. Phys. Eng. Sci.* **464**, 3089–3106 (2008).
- [28] J. Surace and L. Tagliacozzo, Fermionic Gaussian states: an introduction to numerical approaches, *SciPost Phys. Lect. Notes*, 54 (2022).
- [29] G. B. Mbeng, A. Russomanno, and G. E. Santoro, The quantum Ising chain for beginners, *SciPost Phys. Lect. Notes*, 82 (2024).
- [30] A. Paviglianiti, L. Lumia, E. Tirrito, A. Silva, M. Collura, X. Turkeshi, and G. Lami, Emergence of generic entanglement structure in doped matchgate circuits, *Phys. Rev. Lett.* **136**, 020403 (2026).
- [31] M. Oszmaniec, N. Dangniam, M. E. Morales, and Z. Zimborás, Fermion sampling: A robust quantum computational advantage scheme using fermionic linear optics and magic input states, *PRX Quantum* **3**, 020328 (2022).
- [32] S. Boutin and B. Bauer, Quantum impurity models using superpositions of fermionic gaussian states: Practical methods and applications, *Phys. Rev. Res.* **3**, 033188 (2021).
- [33] O. Reardon-Smith, M. Oszmaniec, and K. Korzekwa, Improved simulation of quantum circuits dominated by free fermionic operations, *Quantum* **8**, 1549 (2024).
- [34] B. Dias and R. Koenig, Classical simulation of non-Gaussian fermionic circuits, *Quantum* **8**, 1350 (2024).
- [35] M. Hebenstreit, R. Jozsa, B. Kraus, S. Strelchuk, and M. Yoganathan, All pure fermionic non-gaussian states are magic states for matchgate computations, *Phys. Rev. Lett.* **123**, 080503 (2019).
- [36] J. Cudby and S. Strelchuk, Gaussian decomposition of magic states for matchgate computations (2024), arXiv:2307.12654 [quant-ph].
- [37] O. Reardon-Smith, The fermionic linear optical extent is multiplicative for 4 qubit parity eigenstates (2024), arXiv:2407.20934 [quant-ph].
- [38] L. Bittel, A. A. Mele, J. Eisert, and L. Leone, Optimal trace-distance bounds for free-fermionic states: Testing and improved tomography, *PRX Quantum* **6**, 030341 (2025).
- [39] S. Hakkaku, Y. Tashima, K. Mitarai, W. Mizukami, and K. Fujii, Quantifying fermionic nonlinearity of quantum circuits, *Phys. Rev. Res.* **4**, 043100 (2022).
- [40] A. D. Gottlieb and N. J. Mauser, New measure of electron correlation, *Phys. Rev. Lett.* **95**, 123003 (2005).
- [41] A. D. Gottlieb and N. J. Mauser, Properties of non-freeness: An entropy measure of electron correlation, *International Journal of Quantum Information* **05**, 815 (2007).
- [42] L. Lumia, E. Tirrito, R. Fazio, and M. Collura, Measurement-induced transitions beyond gaussianity: A single particle description, *Phys. Rev. Res.* **6**, 023176 (2024).
- [43] X. Lyu and K. Bu, Fermionic gaussian testing and non-gaussian measures via convolution (2024), arXiv:2409.08180 [quant-ph].
- [44] L. Coffman, G. Smith, and X. Gao, Measuring non-gaussian magic in fermions: Convolution, entropy, and the violation of wick's theorem and the matchgate identity (2025), arXiv:2501.06179 [quant-ph].
- [45] G. Bellomia, A. Amaricci, and M. Capone, Local classical correlations between physical electrons in hubbard systems (2025), arXiv:2506.18709 [cond-mat.str-el].
- [46] P. Sierant, P. Stornati, and X. Turkeshi, Fermionic magic resources of quantum many-body systems, *PRX Quantum* **7**, 010302 (2026).
- [47] L. Amico, R. Fazio, A. Osterloh, and V. Vedral, Entanglement in many-body systems, *Rev. Mod. Phys.* **80**, 517 (2008).
- [48] J. Eisert, M. Cramer, and M. B. Plenio, Colloquium: Area laws for the entanglement entropy, *Rev. Mod. Phys.* **82**, 277 (2010).
- [49] N. Laflorencie, Quantum entanglement in condensed matter systems, *Physics Reports* **646**, 1 (2016), quantum entanglement in condensed matter systems.
- [50] P. Calabrese and J. Cardy, Entanglement entropy and quantum field theory, *J. Stat. Mech. Theory Exp.* **2004**, P06002 (2004).
- [51] J. Eisert, M. Friesdorf, and C. Gogolin, Quantum many-body systems out of equilibrium, *Nature Physics* **11**, 124 (2015).
- [52] P. Calabrese and J. Cardy, Entanglement entropy and conformal field theory, *J. Phys. A: Math. Theor.* **42**, 504005 (2009).
- [53] D. A. Abanin, E. Altman, I. Bloch, and M. Serbyn, Colloquium: Many-body localization, thermalization, and entanglement, *Rev. Mod. Phys.* **91**, 021001 (2019).
- [54] C. D. White, C. Cao, and B. Swingle, Conformal field theories are magical, *Phys. Rev. B* **103**, 075145 (2021).
- [55] T. Haug and L. Piroli, Quantifying nonstabilizerness of matrix product states, *Phys. Rev. B* **107**, 035148 (2023).
- [56] P. S. Tarabunga, E. Tirrito, T. Chanda, and M. Dalmonte, Many-body magic via pauli-markov chains—from criticality to gauge theories, *PRX Quantum* **4**, 040317 (2023).
- [57] J. Odavić, T. Haug, G. Torre, A. Hamma, F. Franchini, and S. M. Giampaolo, Complexity of frustration: A new source of non-local non-stabilizerness, *SciPost Phys.* **15**, 131 (2023).
- [58] G. Passarelli, R. Fazio, and P. Lucignano, Nonstabilizerness of permutationally invariant systems, *Phys. Rev. A* **110**, 022436 (2024).
- [59] P. S. Tarabunga and C. Castelnovo, Magic in generalized Rokhsar-Kivelson wavefunctions, *Quantum* **8**, 1347 (2024).
- [60] P. R. N. Falcão, P. S. Tarabunga, M. Frau, E. Tirrito, J. Zakrzewski, and M. Dalmonte, Nonstabilizerness in U(1) lattice gauge theory, *Phys. Rev. B* **111**, L081102 (2025).
- [61] B. Jasser, J. Odavić, and A. Hamma, Stabilizer entropy and entanglement complexity in the sachdev-ye-kitaev model, *Phys. Rev. B* **112**, 174204 (2025).
- [62] S. Bera and M. Schirò, Non-stabilizerness of Sachdev-Ye-Kitaev model, *SciPost Phys.* **19**, 159 (2025).
- [63] D. Rattacaso, L. Leone, S. F. E. Oliviero, and A. Hamma, Stabilizer entropy dynamics after a quantum quench, *Phys. Rev. A* **108**, 042407 (2023).
- [64] X. Turkeshi, A. Dymarsky, and P. Sierant, Pauli spectrum and nonstabilizerness of typical quantum many-body states, *Phys. Rev. B* **111**, 054301 (2025).
- [65] X. Turkeshi, E. Tirrito, and P. Sierant, Magic spreading in random quantum circuits, *Nat. Commun.* **16**, 2575 (2025).
- [66] E. Tirrito, X. Turkeshi, and P. Sierant, Anticoncen-

- tration and nonstabilizerness spreading under ergodic quantum dynamics, *Phys. Rev. Lett.* **135**, 220401 (2025).
- [67] J. Odavić, M. Viscardi, and A. Hamma, Stabilizer entropy in nonintegrable quantum evolutions, *Phys. Rev. B* **112**, 104301 (2025).
- [68] T. Haug, L. Aolita, and M. Kim, Probing quantum complexity via universal saturation of stabilizer entropies, *Quantum* **9**, 1801 (2025).
- [69] J. A. Montañà López and P. Kos, Exact solution of long-range stabilizer Rényi entropy in the dual-unitary xxz model*, *J. Phys. A: Math. Theor.* **57**, 475301 (2024).
- [70] G. C. Santra, A. Windey, S. Bandyopadhyay, A. Legramandi, and P. Hauke, Complexity transitions in chaotic quantum systems (2025), arXiv:2505.09707 [quant-ph].
- [71] M. Bejan, P. W. Claeys, and J. Yao, Magic spreading under unitary Clifford dynamics (2025), arXiv:2511.21487 [quant-ph].
- [72] E. Tirrito, P. S. Tarabunga, D. S. Bhakuni, M. Dalmonte, P. Sierant, and X. Turkeshi, Universal spreading of nonstabilizerness and quantum transport (2025), 2506.12133 [quant-ph].
- [73] G. Passarelli, A. Russomanno, and P. Lucignano, Nonstabilizerness of a boundary time crystal, *Phys. Rev. A* **111**, 062417 (2025).
- [74] Z.-Y. Hou, C. Cao, and Z.-C. Yang, Stabilizer entanglement as a magic highway (2025), arXiv:2503.20873 [quant-ph].
- [75] P. R. N. Falcão, P. Sierant, J. Zakrzewski, and E. Tirrito, Nonstabilizerness dynamics in many-body localized systems, *Phys. Rev. Lett.* **135**, 240404 (2025).
- [76] T. Hernández-Yanes, P. Sierant, J. Zakrzewski, and M. Płodzień, Nonstabilizerness in quantum-enhanced metrological protocols, *Phys. Rev. A* **113**, 012416 (2026).
- [77] H. Lóio, G. Lami, L. Leone, M. McGinley, X. Turkeshi, and J. D. Nardis, Quantum state designs via magic teleportation (2026), arXiv:2510.13950 [quant-ph].
- [78] G. C. Santra, J. Mildenberger, E. Ballini, A. Bottarelli, M. M. Wauters, and P. Hauke, Quantum resources in non-abelian lattice gauge theories: Nonstabilizerness, multipartite entanglement, and fermionic non-gaussianity (2025), arXiv:2510.07385 [quant-ph].
- [79] M. Rigol, V. Dunjko, and M. Olshanii, Thermalization and its mechanism for generic isolated quantum systems, *Nature* **452**, 854 (2008).
- [80] L. D’Alessio, Y. Kafri, A. Polkovnikov, and M. Rigol, From quantum chaos and eigenstate thermalization to statistical mechanics and thermodynamics, *Adv. Phys.* **65**, 239 (2016).
- [81] S. Aditya, X. Turkeshi, and P. Sierant, Growth and spreading of quantum resources under random circuit dynamics (2025), arXiv:2512.14827 [quant-ph].
- [82] R. Nandkishore and D. A. Huse, Many-Body Localization and Thermalization in Quantum Statistical Mechanics, *Annu. Rev. Condens. Matter Phys.* **6**, 15 (2015).
- [83] F. Alet and N. Laflorencie, Many-body localization: An introduction and selected topics, *C. R. Phys.* **19**, 498 (2018).
- [84] P. Sierant, M. Lewenstein, A. Scardicchio, L. Vidmar, and J. Zakrzewski, Many-body localization in the age of classical computing, *Reports on Progress in Physics* **88**, 026502 (2025).
- [85] L. F. Santos, Integrability of a disordered Heisenberg spin-1/2 chain, *Journal of Physics A: Mathematical and General* **37**, 4723 (2004).
- [86] V. Oganesyan and D. A. Huse, Localization of interacting fermions at high temperature, *Phys. Rev. B* **75**, 155111 (2007).
- [87] A. Pal and D. A. Huse, Many-body localization phase transition, *Phys. Rev. B* **82**, 174411 (2010).
- [88] A. De Luca and A. Scardicchio, Ergodicity breaking in a model showing many-body localization, *Europhysics Letters* **101**, 37003 (2013).
- [89] D. J. Luitz, N. Laflorencie, and F. Alet, Many-body localization edge in the random-field Heisenberg chain, *Phys. Rev. B* **91**, 081103 (2015).
- [90] R. K. Panda, A. Scardicchio, M. Schulz, S. R. Taylor, and M. Žnidarič, Can we study the many-body localisation transition?, *Europhysics Letters* **128**, 67003 (2020).
- [91] J. Šuntajs, J. Bonča, T. Prosen, and L. Vidmar, Ergodicity breaking transition in finite disordered spin chains, *Phys. Rev. B* **102**, 064207 (2020).
- [92] P. Jordan and E. Wigner, Über das paulische Äquivalenzverbot, *Zeitschrift für Physik* **47**, 631 (1928).
- [93] Form of \hat{H}_{xx} in terms of Majorana fermions and A^{xx} matrix are given in End Matter.
- [94] J. Williamson, On the algebraic problem concerning the normal forms of linear dynamical systems, *Am. J. Math.* **58**, 141 (1936).
- [95] B. Zumino, Normal forms of complex matrices, *J. Math. Phys.* **3**, 1055 (1962).
- [96] J. W. Negele, *Quantum many-particle systems* (CRC Press, 2018).
- [97] A. Zhao, N. C. Rubin, and A. Miyake, Fermionic partial tomography via classical shadows, *Phys. Rev. Lett.* **127**, 110504 (2021).
- [98] K. Wan, W. J. Huggins, J. Lee, and R. Babbush, Matchgate shadows for fermionic quantum simulation, *Commun. Math. Phys.* **404**, 629 (2023).
- [99] J. Denzler, A. A. Mele, E. Derbyshire, T. Guaita, and J. Eisert, Learning fermionic correlations by evolving with random translationally invariant hamiltonians, *Phys. Rev. Lett.* **133**, 240604 (2024).
- [100] J. Majksak, D. McNulty, and M. Oszmaniec, A simple and efficient joint measurement strategy for estimating fermionic observables and hamiltonians, *npj Quantum Info.* **11**, 61 (2025).
- [101] P. Sierant, M. Lewenstein, and J. Zakrzewski, Polynomially filtered exact diagonalization approach to many-body localization, *Phys. Rev. Lett.* **125**, 156601 (2020).
- [102] B. Bauer and C. Nayak, Area laws in a many-body localized state and its implications for topological order, *Journal of Statistical Mechanics: Theory and Experiment* **2013**, P09005 (2013).
- [103] M. Serbyn, Z. Papić, and D. A. Abanin, Local conservation laws and the structure of the many-body localized states, *Phys. Rev. Lett.* **111**, 127201 (2013).
- [104] D. A. Huse, R. Nandkishore, and V. Oganesyan, Phenomenology of fully many-body-localized systems, *Phys. Rev. B* **90**, 174202 (2014).
- [105] J. Niedda, G. B. Testasecca, G. Magnifico, F. Balducci, C. Vanoni, and A. Scardicchio, Renormalization group analysis of the many-body localization transition in the random-field xxz chain, *Physical Review B* **112**, 144201 (2025).

- [106] Detailed analysis of ergodic-MLB crossover in the impurity model with standard ergodicity breaking indicators is performed in [160].
- [107] P. W. Anderson, Absence of diffusion in certain random lattices, *Phys. Rev.* **109**, 1492 (1958).
- [108] F. Evers and A. D. Mirlin, Anderson transitions, *Rev. Mod. Phys.* **80**, 1355 (2008).
- [109] L. Vidmar, B. Krajewski, J. Bonča, and M. Mierzejewski, Phenomenology of spectral functions in disordered spin chains at infinite temperature, *Phys. Rev. Lett.* **127**, 230603 (2021).
- [110] B. Krajewski, L. Vidmar, J. Bonča, and M. Mierzejewski, Restoring ergodicity in a strongly disordered interacting chain, *Phys. Rev. Lett.* **129**, 260601 (2022).
- [111] V. Ros, M. Mueller, and A. Scardicchio, Integrals of motion in the many-body localized phase, *Nuclear Physics B* **891**, 420 (2015).
- [112] J. Z. Imbrie, On many-body localization for quantum spin chains, *Journal of Statistical Physics* **163**, 998 (2016).
- [113] W. D. Roeck, L. Giacomin, F. Huveneers, and O. Prosnik, *Absence of normal heat conduction in strongly disordered interacting quantum chains* (2024), arXiv:2408.04338 [math-ph].
- [114] B. Villalonga and B. K. Clark, Eigenstates hybridize on all length scales at the many-body localization transition (2020), arXiv:2005.13558.
- [115] S. J. Garratt, S. Roy, and J. T. Chalker, Local resonances and parametric level dynamics in the many-body localized phase, *Phys. Rev. B* **104**, 184203 (2021).
- [116] P. J. D. Crowley and A. Chandran, A constructive theory of the numerically accessible many-body localized to thermal crossover, *SciPost Phys.* **12**, 201 (2022).
- [117] J. Colbois, F. Alet, and N. Laflorencie, Interaction-driven instabilities in the random-field xxz chain, *Physical Review Letters* **133**, 116502 (2024).
- [118] J. Colbois, F. Alet, and N. Laflorencie, Statistics of systemwide correlations in the random-field xxz chain: Importance of rare events in the many-body localized phase, *Phys. Rev. B* **110**, 214210 (2024).
- [119] N. Laflorencie, J. Colbois, and F. Alet, Cat states carrying long-range correlations in the many-body localized phase, *Phys. Rev. B* **112**, 224207 (2025).
- [120] A. Morningstar, L. Colmenarez, V. Khemani, D. J. Luitz, and D. A. Huse, Avalanches and many-body resonances in many-body localized systems, *Phys. Rev. B* **105**, 174205 (2022).
- [121] H. Ha, A. Morningstar, and D. A. Huse, Many-body resonances in the avalanche instability of many-body localization, *Phys. Rev. Lett.* **130**, 250405 (2023).
- [122] A. Padhan, J. Colbois, F. Alet, and N. Laflorencie, *Long-range resonances in quasiperiodic many-body localization* (2025), arXiv:2510.24704 [cond-mat.dis-nn].
- [123] See Supplementary Material at [URL will be inserted by publisher] for further details on the relation between cat eigenstates and fermionic antiflatness. It contains Refs. [114–121, 161–164].
- [124] G. De Chiara, S. Montangero, P. Calabrese, and R. Fazio, Entanglement entropy dynamics of heisenberg chains, *Journal of Statistical Mechanics: Theory and Experiment* **2006**, P03001 (2006).
- [125] M. Serbyn, Z. Papić, and D. A. Abanin, Universal slow growth of entanglement in interacting strongly disordered systems, *Phys. Rev. Lett.* **110**, 260601 (2013).
- [126] M. Žnidarič, T. Prosen, and P. Prelovšek, Many-body localization in the Heisenberg XXZ magnet in a random field, *Phys. Rev. B* **77**, 064426 (2008).
- [127] M. Žnidarič, Entanglement in a dephasing model and many-body localization, *Phys. Rev. B* **97**, 214202 (2018).
- [128] J. H. Bardarson, F. Pollmann, and J. E. Moore, Unbounded growth of entanglement in models of many-body localization, *Phys. Rev. Lett.* **109**, 017202 (2012).
- [129] S. Iyer, V. Oganesyan, G. Refael, and D. A. Huse, Many-body localization in a quasiperiodic system, *Phys. Rev. B* **87**, 134202 (2013).
- [130] E. V. H. Doggen and A. D. Mirlin, Many-body delocalization dynamics in long aubry-andré quasiperiodic chains, *Phys. Rev. B* **100**, 104203 (2019).
- [131] U. Agrawal, S. Gopalakrishnan, and R. Vasseur, Universality and quantum criticality in quasiperiodic spin chains, *Nature Communications* **11**, 2225 (2020).
- [132] A. S. Aramthottil, T. Chanda, P. Sierant, and J. Zakrzewski, Finite-size scaling analysis of the many-body localization transition in quasiperiodic spin chains, *Phys. Rev. B* **104**, 214201 (2021).
- [133] P. R. N. Falcão, A. S. Aramthottil, P. Sierant, and J. Zakrzewski, Many-body localization crossover is sharper in a quasiperiodic potential, *Phys. Rev. B* **110**, 184209 (2024).
- [134] M. Schulz, C. A. Hooley, R. Moessner, and F. Pollmann, Stark many-body localization, *Phys. Rev. Lett.* **122**, 040606 (2019).
- [135] E. van Nieuwenburg, Y. Baum, and G. Refael, From bloch oscillations to many-body localization in clean interacting systems, *Proceedings of the National Academy of Sciences* **116**, 9269 (2019), <https://www.pnas.org/doi/pdf/10.1073/pnas.1819316116>.
- [136] S. R. Taylor, M. Schulz, F. Pollmann, and R. Moessner, Experimental probes of stark many-body localization, *Phys. Rev. B* **102**, 054206 (2020).
- [137] T. Chanda, R. Yao, and J. Zakrzewski, Coexistence of localized and extended phases: Many-body localization in a harmonic trap, *Phys. Rev. Res.* **2**, 032039 (2020).
- [138] R. Yao and J. Zakrzewski, Many-body localization of bosons in an optical lattice: Dynamics in disorder-free potentials, *Phys. Rev. B* **102**, 104203 (2020).
- [139] R. Yao, T. Chanda, and J. Zakrzewski, Nonergodic dynamics in disorder-free potentials, *Annals of Physics* **435**, 168540 (2021), special Issue on Localisation 2020.
- [140] R. Yao, T. Chanda, and J. Zakrzewski, Many-body localization in tilted and harmonic potentials, *Phys. Rev. B* **104**, 014201 (2021).
- [141] J. A. Kjäll, J. H. Bardarson, and F. Pollmann, Many-body localization in a disordered quantum ising chain, *Phys. Rev. Lett.* **113**, 107204 (2014).
- [142] A. S. Aramthottil, P. Sierant, M. Lewenstein, and J. Zakrzewski, Phenomenology of many-body localization in bond-disordered spin chains, *Phys. Rev. Lett.* **133**, 196302 (2024).
- [143] X. Li, D.-L. Deng, Y.-L. Wu, and S. Das Sarma, Statistical bubble localization with random interactions, *Phys. Rev. B* **95**, 020201 (2017).
- [144] M. Serbyn, D. A. Abanin, and Z. Papić, Quantum many-body scars and weak breaking of ergodicity, *Nature Physics* **17**, 675 (2021).
- [145] S. Moudgalya, B. A. Bernevig, and N. Regnault, Quantum many-body scars and hilbert space fragmentation:

- A review of exact results, *Reports on Progress in Physics* **85**, 086501 (2022).
- [146] T. Szöldra, P. Sierant, M. Lewenstein, and J. Zakrzewski, Unsupervised detection of decoupled subspaces: Many-body scars and beyond, *Phys. Rev. B* **105**, 224205 (2022).
- [147] A. S. Aramthottil, U. Bhattacharya, D. González-Cuadra, M. Lewenstein, L. Barbiero, and J. Zakrzewski, Scar states in deconfined z_2 lattice gauge theories, *Phys. Rev. B* **106**, L041101 (2022).
- [148] A. Chandran, T. Iadecola, V. Khemani, and R. Moessner, Quantum many-body scars: A quasiparticle perspective, *Annual Review of Condensed Matter Physics* **14**, 443 (2023).
- [149] M. Brenes, M. Dalmonte, M. Heyl, and A. Scardicchio, Many-body localization dynamics from gauge invariance, *Phys. Rev. Lett.* **120**, 030601 (2018).
- [150] T. Rakovszky, P. Sala, R. Verresen, M. Knap, and F. Pollmann, Statistical localization: From strong fragmentation to strong edge modes, *Phys. Rev. B* **101**, 125126 (2020).
- [151] M. Serbyn, Z. Papić, and D. A. Abanin, Quantum quenches in the many-body localized phase, *Phys. Rev. B* **90**, 174302 (2014).
- [152] A. Prakash, J. Pixley, and M. Kulkarni, Universal spectral form factor for many-body localization, *Phys. Rev. Res.* **3**, L012019 (2021).
- [153] D. Aceituno Chávez, C. Artiaco, T. Klein Kvorning, L. Herviou, and J. H. Bardarson, Ultraslow growth of number entropy in an 1-bit model of many-body localization, *Phys. Rev. Lett.* **133**, 126502 (2024).
- [154] V. Berger, A. Nava, J. H. Bardarson, and C. Artiaco, Numerical study of disordered noninteracting chains coupled to a local Lindblad bath (2024), [arXiv:2412.03233 \[cond-mat.dis-nn\]](https://arxiv.org/abs/2412.03233).
- [155] T. Szöldra, P. Sierant, M. Lewenstein, and J. Zakrzewski, Catching thermal avalanches in the disordered XXZ model, *Phys. Rev. B* **109**, 134202 (2024).
- [156] A. Scocco, G. Passarelli, M. Collura, P. Lucignano, and A. Russomanno, Thermalization propagation front and robustness against avalanches in localized systems, *Phys. Rev. B* **110**, 134204 (2024).
- [157] A. Chandran, I. H. Kim, G. Vidal, and D. A. Abanin, Constructing local integrals of motion in the many-body localized phase, *Phys. Rev. B* **91**, 085425 (2015).
- [158] A. K. Kulshreshtha, A. Pal, T. B. Wahl, and S. H. Simon, Behavior of 1-bits near the many-body localization transition, *Phys. Rev. B* **98**, 184201 (2018).
- [159] N. Laflorencie, G. Lemarié, and N. Macé, Chain breaking and Kosterlitz-Thouless scaling at the many-body localization transition in the random-field Heisenberg spin chain, *Phys. Rev. Research* **2**, 042033 (2020).
- [160] P. R. N. Falcão *et al.*, To appear.
- [161] D. J. Luitz, Long tail distributions near the many-body localization transition, *Phys. Rev. B* **93**, 134201 (2016).
- [162] P. Sierant and J. Zakrzewski, Level statistics across the many-body localization transition, *Phys. Rev. B* **99**, 104205 (2019).
- [163] D. J. Luitz and Y. B. Lev, Absence of slow particle transport in the many-body localized phase, *Phys. Rev. B* **102**, 100202 (2020).
- [164] J. Gray, S. Bose, and A. Bayat, Many-body localization transition: Schmidt gap, entanglement length, and scaling, *Phys. Rev. B* **97**, 201105 (2018).

Supplementary material: Fermionic magic resources in disordered quantum spin chains

In this supplementary material, we provide additional details on the relationship between cat eigenstates and fermionic antiflatness.

Relation between cat MBL eigenstates and the FAF

In the main letter, we show that for the $|\Psi_{\text{cat}}^{\pm}\rangle$ eigenstates [see Eq. (5)], the fermionic antiflatness isolates the contribution of the cat component and provides a proxy for the number of resonant spins. Here, we extend the analysis by showing that the dominant cat eigenstates are most often associated with four-site resonances, resulting in a peak in the probability distribution at $\mathcal{F}_1 \approx 4$, independent of the system size.

Figure S.1 shows the probability distribution of \mathcal{F}_1 for midspectrum eigenstates of the XXZ Hamiltonian for different disorder strengths W and system sizes L . In the simulations, we set $\Delta = 1$ and average the results over at least 10^3 disorder realizations. In the ergodic regime ($W = 1$), the position of the mode of $\mathcal{P}(\mathcal{F}_1)$ shifts linearly with L , as illustrated in Fig. S.1(a), highlighting the extensive nature of the FAF for ergodic eigenstates. Increasing the disorder strength leads to a qualitative

change in the distribution, with the emergence of a long tail extending to extremely low values of \mathcal{F}_1 . The relative weight of such eigenstates grows with W , resulting in a broad distribution at $W = 3$, as shown in Fig. S.1(b). Similar broad distributions have already been reported for several observables [161–164], and they are a hallmark of the ETH-MBL crossover.

At strong disorder $W = 8$, the distribution changes markedly. The primary peak shifts towards $\mathcal{F}_1 \approx 0$, while a secondary peak emerges at $\mathcal{F}_1 \approx 4$, independent of the system size. In addition, the tail of the distribution decays exponentially towards extensive values of the FAF, as seen in Fig. S.1(c). The tail is strongly suppressed upon the further increase of W , and the peak at $\mathcal{F}_1 \approx 4$ becomes more pronounced, as illustrated in Fig. S.1(d).

The structure of these distributions closely parallels that of the entanglement entropy, where analogous peaks have been attributed to the existence of resonant eigenstates [161]. Since the FAF directly probes the number of resonant spins present in the MBL eigenstates of the form of Eq. (5), the distribution shown in the bottom panel of Fig. S.1 suggests that these resonances most commonly involve four spins.

Figure S.2 illustrates the on-site magnetization profiles

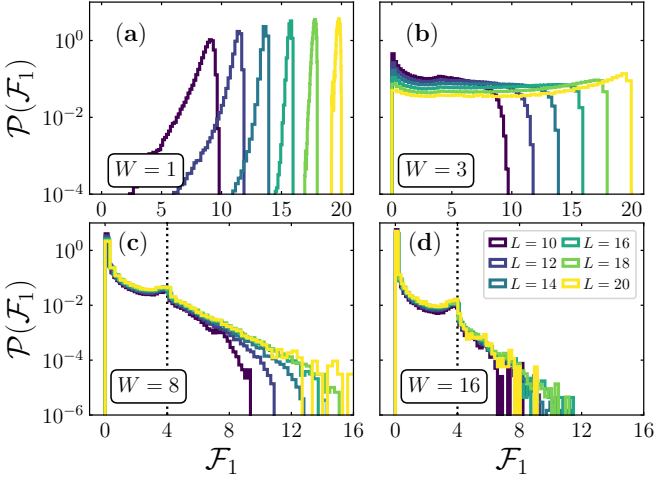


Figure S.1. Probability distribution \mathcal{F}_1 for different disorder strengths W and system sizes L . For $W = 1$ [panel (a)], the distribution is approximately Gaussian, with its modes shifting linearly with L . For $W = 3$ [panel (b)], the distribution becomes broad, a hallmark of the ETH-MBL crossover. In the MBL regime ($W > 5$) [panels (c-d)], it develops a secondary peak near $\mathcal{F}_1 \approx 4$, and its tail decays exponentially, regardless of the system size.

of four eigenstates obtained from different disorder realizations, selected such that $\mathcal{F}_1 = [4-\epsilon, 4+\epsilon]$, with $\epsilon = 10^{-3}$. In the numerical simulations, we consider $L = 18$ and $W = 16$, placing the system deep in the MBL regime. The selected states follow the structure of the ansatz described in Eq. (5): spins participating in the resonant state $|\varphi\rangle$ exhibit $\langle\hat{\sigma}_i^z\rangle \approx 0$, while the remaining spins are practically frozen, with $\langle\hat{\sigma}_i^z\rangle \approx \pm 1$. Moreover, the half-chain entanglement entropy is close to $\ln 2$, providing strong evidence for the cat-like structure of these eigenstates.

The hypothesis that states with $\mathcal{F}_1 \approx 4$ consist of a tensor product between a cat-like state with four spins and a configuration with $L-4$ spins “frozen”, i.e., $\langle\hat{\sigma}_i^z\rangle = \pm 1$, should be tested on more quantitative grounds. This picture is idealized and does not apply to all states with $\mathcal{F}_1 \approx 4$. In practice, deviations become more pronounced as the system size L and the tolerance ϵ increases. However, as we show below, the validity of this picture improves with increasing disorder strength.

To quantify how many spins are effectively “melted” in a given MBL eigenstate, we introduce the observable

$$\mathcal{R}(|\Psi\rangle) = L - \sum_{i=1}^L |\langle\Psi|\hat{\sigma}_i^z|\Psi\rangle| \quad (\text{S.1})$$

which directly counts the number of spins with non-saturated magnetization. Therefore, evaluating this observable for eigenstates with $\mathcal{F}_1 \approx 4$ provides a quantitative measure of how many spins are participating in the structure $|\varphi\rangle$, defined in Eq. (5).

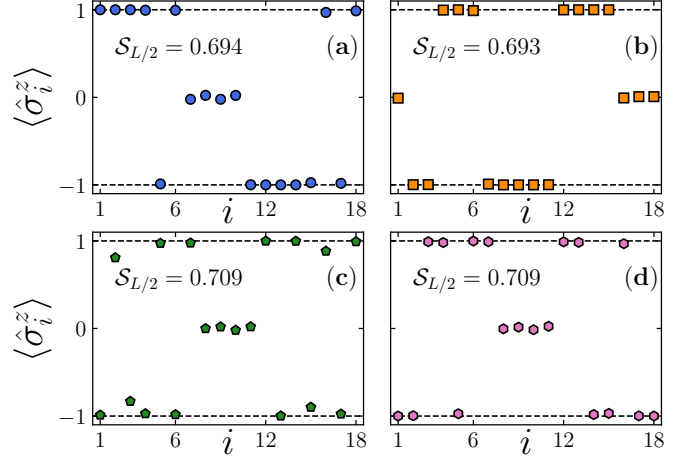


Figure S.2. On-site spin magnetization profiles $\langle\hat{\sigma}_i^z\rangle$ of four different eigenstates with $\mathcal{F}_1 = 4 \pm \epsilon$, where $\epsilon = 10^{-3}$. The simulations are performed for $W = 16$, $\Delta = 1$, and $L = 18$. The states follow the ansatz of Eq. (5), consisting of a four-spin resonant cluster and $L-4$ spins having frozen configurations. The half-chain entanglement entropy is close to $\mathcal{S}_{L/2} \approx \ln 2$, providing evidence for the cat-like structure of such states.

In the top row of Fig. S.3, we show the probability distribution $\mathcal{P}(\mathcal{R})$ for the states satisfying $\mathcal{F}_1 \in [4-\epsilon, 4+\epsilon]$, for two representative disorder strengths, $W = 8$ and $W = 16$, and several values of tolerance ϵ . All data are obtained at a fixed system size $L = 16$ and interaction strength $\Delta = 1$. For $W = 8$, shown in Fig. S.3(a), the distribution exhibits a maximum near $\mathcal{R} \approx 4$, indicating that resonances are more likely to involve four spins, while the remaining spins are frozen. However, the distribution remains very broad towards larger values of \mathcal{R} , and its dependence on the tolerance ϵ is relatively weak. This behavior reflects the presence of additional, weakly delocalized states at intermediate disorder.

Increasing the disorder strength to $W = 16$ leads to a sharper peak at $\mathcal{R} \approx 4$, which increases as the tolerance decreases, with a pronounced maximum for $\epsilon = 10^{-3}$. Simultaneously, the probability weight for $\mathcal{R} < 4$ is suppressed, indicating that states involving fewer than four resonant spins become increasingly rare deep in the MBL regime.

The bottom row of Fig. S.3 illustrates the system-size dependence of $\mathcal{P}(\mathcal{R})$ for a fixed tolerance $\epsilon = 10^{-3}$. For $W = 8$, shown in Fig. S.3(c), the distribution still peaks at $\mathcal{R} = 4$ for all system sizes considered here. While the probability of having $\mathcal{R} < 4$ becomes significantly small when L increases, the weight of having $\mathcal{R} > 4$ grows. Similar behavior is observed for $W = 16$, where the relative weight of having $\mathcal{R} \approx 4$ decreases with L . Nevertheless, this peak at $\mathcal{R} \approx 4$ remains significantly more pronounced than for any other values, supporting the hypothesis that most of the eigenstates having $\mathcal{F}_k \approx 4$ consist of four resonant spins embedded in a frozen background.

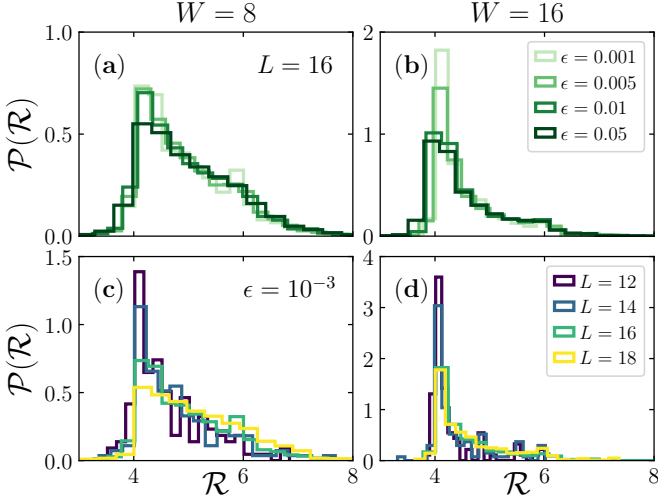


Figure S.3. (a-b) Probability distribution $\mathcal{P}(\mathcal{R})$ for eigenstates with $\mathcal{F}_1 \in [4-\epsilon, 4+\epsilon]$ for several values of ϵ , at disorder strengths $W = 8$ and $W = 16$, respectively. Numerical calculations are performed for $L = 16$ and $\Delta = 1$. The distribution \mathcal{P} peaks near $\mathcal{R} \approx 4$ and becomes narrower with increasing disorder strength and decreasing tolerance ϵ , consistent with a picture of four effectively delocalized spins. (c-d) Probability distribution of \mathcal{R} for different system sizes L at a fixed tolerance $\epsilon = 10^{-3}$. The peak at $\mathcal{R} \approx 4$ persists for all L , while increasing system size mainly affect the tail at $\mathcal{R} > 4$.

Although short-range resonances constitute the most common type of cat-like MBL eigenstates, rare long-range many-body resonances have attracted significant attention in recent years, as they have been argued to potentially destabilize the MBL regime [114–121]. In particular, system-wide resonances take the form of Eq. (5) and, as shown in Ref. [119], can be identified through their spin-spin correlations. Specifically, their longitudinal connected correlator

$$C_{i,i+L/2}^{zz} = |\langle \hat{\sigma}_i^z \hat{\sigma}_{i+L/2}^z \rangle - \langle \hat{\sigma}_i^z \rangle \langle \hat{\sigma}_{i+L/2}^z \rangle| \quad (\text{S.2})$$

remains $\mathcal{O}(1)$ for $W \gg 1$, whereas typical MBL eigenstates have a vanishing connected correlator.

Figure 3 shows such rare cat eigenstates in the XXZ model for two different disorder realizations deep in the MBL regime ($W = 16$), with $\Delta = 1$ and $L = 14$. In panels (a-b), we show the maximal longitudinal connected correlators $C_{i,i+L/2}^{zz}$, maximized over all spin pairs $(i, i+L/2)$, for several eigenstates. Typical MBL eigenstates exhibit vanishing correlators, $C_{i,i+L/2}^{zz} \approx 0$, as indicated by the black dots. In contrast, a pair of eigenstates (colored markers) exhibits anomalously strong correlations, with $C_{i,i+L/2}^{zz} \approx 1$. These states appear as quasi-degenerate pairs, as evidenced by their small energy gap δe , where e is the energy density. In the insets, we show the specific spin pair responsible for such high correlations, while the other remains close to zero.

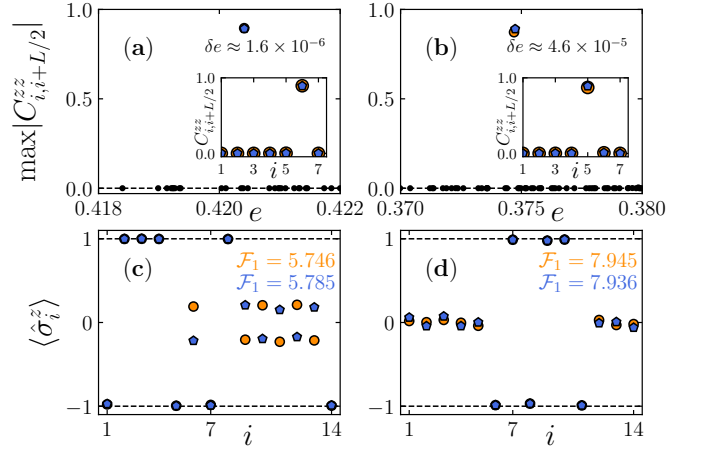


Figure S.4. Long-range cat eigenstates in the XXZ model for $W = 16$ and $L = 14$. (a-b) The cat eigenstates exhibit significantly higher long-range connected longitudinal correlations $C_{i,i+L/2}^{zz}$ compared to typical MBL eigenstates and appear as quasi-degenerate pairs. (c-d) On-site magnetization $\langle \hat{\sigma}_i^z \rangle$ of the corresponding cat eigenstates shown in panels (a) and (b), respectively. The value of \mathcal{F}_1 provides a proxy for the number of spins participating in the cat-structure.

In panels (c-d) of Fig. S.4, we show the spin magnetization profile $\langle \Psi_{\text{cat}}^{\pm} | \hat{\sigma}_i^z | \Psi_{\text{cat}}^{\pm} \rangle$ of these eigenstates. Panel (c) corresponds to the cat eigenstates highlighted in panel (a). Although the structure of $|\Psi_{\text{cat}}^{\pm}\rangle$ does not correspond to an equal superposition of the hybridized product states, the value of \mathcal{F}_1 still provides a reliable proxy for the number of spins participating in the cat structure, with $\mathcal{F}_1 \approx 6$. This relation is more visible in panel (d), which shows the magnetization profiles of the cat eigenstates displayed in panel (b). In this case, the resonant spins follow an approximately equal superposition, with $\mathcal{F}_1 \approx 8$, consistent with the number of spins participating

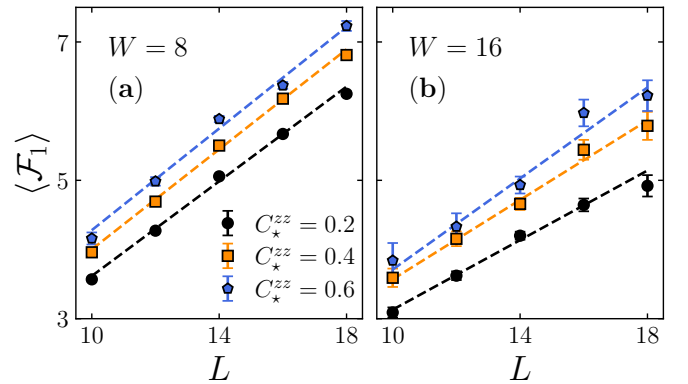


Figure S.5. System-size dependence of the average value of the FAF $\langle \mathcal{F}_1 \rangle$ of the long-range cat eigenstates for (a) $W = 8$ and (b) $W = 16$, and several values of the correlation threshold C_*^{zz} . The average value grows approximately linearly with the system size, with the value of $\langle \mathcal{F}_1 \rangle$ being comparable to the number of fluctuating sites in the cat-like eigenstates.

in the cat-like resonance.

As shown in Fig. S.4, the number of spins participating in the long-range cat eigenstates differs from that of the short-range resonances and can be extensively large. In Fig.17 of Ref. [119], the authors demonstrated that the number of fluctuating sites of $|\Psi_{\text{cat}}^{\pm}\rangle$ increases approximately linearly with the system size, with a slope that depends on the disorder strength W . Since the fermionic antiflatness \mathcal{F}_1 probes the number of fluctuating spins, its average behavior is expected to exhibit similar behavior.

In Fig. S.5, we show the system-size dependence of the average FAF $\langle \mathcal{F}_1 \rangle$ for the long-range cat eigenstates in the middle of the spectrum. These states are identified

by selecting quasi-degenerate pairs of eigenstates with a longitudinal connected correlator $C^{zz} \geq C_{\star}^{zz}$, for three threshold values, $C_{\star}^{zz} = 0.2, 0.4, 0.6$. The average value of $\langle \mathcal{F}_1 \rangle$ increases roughly linearly with L . For $W = 8$, the slope of the linear scaling ($aL + b$) is approximately constant, with $a \approx 0.36$. For $W = 16$, the statistics are poorer due to the strong suppression of cat states, with the slopes depending more sensitively on the choice of $C^{zz} \geq C_{\star}^{zz}$. Nevertheless, the values of the fermionic antiflatness are comparable to the number of fluctuating sites reported in Ref. [119], further supporting the idea that the FAF is a proxy for the number of spins participating in the resonance.